Korean J. Chem. Eng., 40(9), 2239-2252 (2023)
DOI: 10.1007/s11814-023-1408-0

pISSN: 0256-1115
eISSN: 1975-7220

Low-temperature synthesis and characterization of porous chromium terephthalate MIL-101(Cr) and its photocatalytic degradation of phenanthrene

Usman Abubakar Adamu[*,], Noor Hana Hanif Abu Bakar[*,†], Zakariyya Uba Zango[***], Nonni Soraya Sambudi[****,*****], Anwar Iqbal[*], Mohd Hazwan Hussin[*], and Tuan Sherwyn Hamidon[*]**

*Nanoscience Research Laboratory, School of Chemical Sciences, Universiti Sains Malaysia, 11800 Penang, Malaysia
**Department of Chemistry, Faculty of Sciences, Gombe State University, P.M.B. 127, Gombe, Nigeria
***College of Natural and Applied Sciences, Al-Qalam University Katsina, 2137, Katsina State, Nigeria
****Chemical Engineering Department, Universiti Teknologi PETRONAS, Seri Iskandar, Perak, Malaysia
*****Department of Chemical Engineering, Faculty of Technological Industry, Universitas Pertamina, Simprug, Jakarta 12220, Indonesia

(*Received 15 June 2022 • Revised 27 January 2023 • Accepted 27 February 2023*)

Abstract−Low-temperature hydrothermal technique was employed for the synthesis of highly porous and crystalline MIL-101(Cr) metal-organic frameworks series. The resulting as-synthesized MOFs were characterized by Fourier transform infrared (FTIR) spectroscopy, powdered X-ray diffraction (XRD), scanning electron microscopy (SEM), nitrogen adsorption-desorption analysis, thermogravimetric analysis (TGA), photoluminescence (PL) spectroscopy, and ultraviolet-visible (UV-vis) diffuse reflectance spectroscopy. The photocatalytic activity of the MOFs was evaluated for degradation of phenanthrene (PHE) under visible light irradiation. Among the MOFs, MIL-101@160 has the highest Brunner Emmett-Teller (BET) specific surface area and corresponding pore volume of 2,592.2 m^2g^{-1} and 1.09 cm^3g^{-1}, respectively. Furthermore, it has shown higher photocatalytic degradation of the PHE than other samples with 98% degradation efficiency achieved within 150 minutes.

Keywords: MIL-101(Cr), Metal-organic Frameworks (MOFs), Surface Area, Photocatalytic Degradation, PAHs, Phenanthrene

INTRODUCTION

Solar energy is significant in the development of numerous technologies for addressing environmental pollution. Among these, photocatalysis has been found to be a non-toxic, readily available, and promising method for water purification [1,2]. Photocatalysts are substances with semiconducting properties that have been generally applied in the degradation of environmental pollutants [3,4]. The heterogeneous photocatalysts have attracted attention due to their potential in the treatment of toxic organic and inorganic pollutants in both aqueous and gas medium. The advanced oxidation process (AOP) is referred to as the process in which the pollutants in water are photo-catalytically degraded into non-toxic forms. The process is initiated by light which acts upon the photocatalyst material by generating free radical species that subsequently attack the pollutants and convert them to non-toxic by-products of CO_2 and water through complete mineralization [3].

Metal-organic frameworks (MOFs), like conventional photocatalysts such as ZnO and TiO_2, can act as semiconductors upon light irradiation. It is a building block of transition metal ion as the central node with the organic moiety as the ligand [4,5]. In photocatalysis, the organic linker usually acts as an antenna that traps light from the source and subsequently activates the metal site through a ligand to metal charge transfer mechanism [6]. The higher surface area and porosity of MOFs compared to the conventional photocatalysts is attributed to the design of the framework, forming three-dimensional structure with higher tunability. Cr containing MOFs poses relatively good stability in aqueous solution and small band gap energies that is capable of light excitation, and therefore is regarded as promising candidate for the treatment of organic contaminants [7].

Among the several MOFs that have been used as photocatalysts in the treatment of organic pollutants are MIL-125(Ti) [8], UiO-66(Zr) [9], UiO-67 [10] and MIL-53(Fe) [11]. The ability of these MOFs in adsorption and photocatalysis has provided a great opportunity in the treatment of wastewater [12]. MIL-101(Cr) has been considered a promising MOF-based photocatalyst with a high surface area and visible light response. It has distinct characteristics such as high surface area, controllable pore size and low density, which makes it possible to be used for adsorption and catalysis [13,14].

Polycyclic aromatic hydrocarbons (PAHs) are ubiquitous organic pollutants produced through natural as well as anthropogenic activity. They are usually formed due to incomplete combustion of organic matter such as crude oil, wood, and coal, and are also generated from industrial activity. PAHs are generally not produced for industrial applications. However, a few are used as intermediaries in photographic, pharmaceutical, and agricultural products. For example, phenanthrene (PHE) is used as intermediary in the manufacture of resins, pesticides, dyes, plastics, and explosives. PAHs are persistent in the environment. When present in water, they hardly degrade

†To whom correspondence should be addressed.
E-mail: hana_hanif@usm.my

because of their solubility and or lipophilic nature [15]. A total of 16 PAHs were identified and included as emerging persistent pollutants in the environment by the United States Environmental Protection Agency (USEPA) and other international environmental regulatory agencies [16]. Thus, progress in the PAHs degradation has been identified as a way forward for environmental remediation. The World Health Organization defines a maximum tolerable limit of 0.2 g/L for total PAHs in drinking water [17], while Global outdoor air concentrations of PAHs range from 5.85 to 1,213 ng/m^3, with a weighted median concentration of 142 ng/m^3 [18].

Over a decade, researchers have focused on the synthesis of MIL-101 for various applications. However, the number of works related to the use of MIL-101 as photocatalyst is still few, despite the good features of the MOFs for such applications [19]. An extensive search on previously synthesized MIL-101 revealed that a vast majority of the researchers applied mineral acids for long durations of time and very high temperatures in the range of 200-220 °C during the synthesis of MIL-101. The most common acids used are hydrofluoric acid (HF), hydrochloric acid (HCl), and nitric acid (HNO_3). As an example, Gobara et al. [20] reported the synthesis of Pt/MIL-101 and Ni/MIL-101 hybrid composites at 220 °C for 9 h using HF for enhanced adsorption performance towards industrial toxic dyes, while Vo and coworkers [21] reported the synthesis of graphite oxide on MIL-101 involving HNO_3, at 200 for 12 h. Similarly, Kavun et al. [22] prepared and modified MIL-101 at 220 °C for the separation and recovery of rare earth elements. In summary, MIL-101(Cr) is usually prepared at relatively high temperatures (220 °C) and requires a very long time for nucleation.

In this work, we therefore aimed at synthesizing and characterizing a series of MIL-101(Cr) at low temperatures of 150, 160, 170, and 180 °C against those synthesized at 200 and 220 °C. The photocatalytic application of the MOFs was tested against degradation of PHE.

MATERIALS AND METHODS

1. Synthesis and Characterization of MIL-101(Cr) Series

MIL-101(Cr) was synthesized according to the procedure described by [23], with some modifications. Typically, 3.20 g of $Cr(NO_3)_3 \cdot 9H_2O$ (8 mmol) was dissolved in 35 mL ultrapure water, and then mixed with an equimolar amount of terephthalic acid (1.32 g, 8 mmol). The above solution was thoroughly stirred using a magnetic stirrer for one hour at room temperature. The homogenized solution was then transferred into a 50 mL Teflon-lined autoclave, sealed, and placed in an oven at 150 °C for 6 h. The solution was allowed to cool at room temperature and the fine crystals were separated from the solution using centrifugation at 3,000 rpm for 20 minutes. The resultant green crystals were washed thoroughly with ethanol three times to remove the unreacted terephthalic acid from the solution. Finally, the MIL-101@150 was then collected from the ethanolic solution by centrifugation at 3,000 rpm for 20 minutes and dried in an oven at 80 °C for three days.

The above procedure was repeated for the synthesis of MIL-101@160, MIL-101@170, MIL-101@180, MIL-101@200, and MIL-101@220 by varying temperatures to 160, 170, 180, 200, and 220 °C, respectively.

Fourier transform infrared (FTIR) spectra were acquired from PerkinElmer Model System 2000 (U.S.A.) by using the potassium bromide (KBr) pellet in the range of 400-4,000 cm^{-1} in determining the functional groups of the MIL-101(Cr) samples. The structural characterizations of the prepared MIL-101(Cr) samples were carried out using a D8 Advance X-ray powder diffractometer (XRD) (Germany) with Cu-Kα radiation (λ_{Kal}=1.5418 Å), and a monochromatic filter in the 2θ range of 0°-30°. The Debye-Scherer formula (Eq. (1)) was used in calculating the average crystalline sizes of the prepared MIL-101(Cr).

$$D=K\lambda/\beta\cos\theta \quad (1)$$

where D is the size of the particle, K is known as the Scherer's constant (K=0.94), λ is the X-ray wavelength (1.54178 Å), β is full width at half maximum (FWHM) of the diffraction peak and is the θ Bragg angle. Thermogravimetric analysis (TGA) of the synthesized MIL-101 samples was carried out using a thermogravimetric analyzer TGA STA 6000 (PerkinElmer) at a heating rate of 20 °C min^{-1} from 30 °C to 800 °C and held for 5 min at 800 °C. The total surface area analyses of the synthesized MIL-101(Cr) samples were carried out using a Micromeritics ASAP 2020 surface adsorption porosimeter with nitrogen. Samples were degassed at 110 °C for 12 h. The specific surface area was analyzed by the Brunauer-Emmett-Teller (BET) method and the pore sizes and volumes were calculated using Barrett, Joyner, and Halenda (BJH) method. Scanning electron microscopy (SEM) analyses were performed to examine the morphology of MIL-101(Cr) samples using a Quanta 650 field emission gun SEM (Holland). The samples were sputter-coated with gold before analysis. The magnifications used in the analysis were 12,000x and 25,000x, while the voltage applied to obtain the images of the desired compounds was 10 kV. The UV-vis diffuse reflectance spectroscopy (UV-Vis DRS) analyses were carried out using a Lambda 35 UV/vis spectrophotometer (PerkinElmer) in the range of 200-800 nm, while photoluminescence (PL) spectra were measured using a PerkinElmer LS 55 fluorescence spectrophotometer. The excitation wavelength for all samples is 380 nm. The K-alpha X-ray photoelectron spectrometer (Thermo Fischer Scientific) was used to determine the chemical elements present in MIL-101@160 and MIL-101@220 photocatalysts.

Before the electrochemical impedance spectroscopy (EIS) of the catalyst could be performed, a working electrode had to be created. To obtain adequate dispersibility, 1 mL of perfluorinated resin solution containing Nafion (5.0 wt%) and 40 mg of the produced catalyst were exposed to sonication for 3 h. Subsequently, 20 µL of the mixture was poured onto an FTO electrode, which was dried overnight at 60 °C.

A Gamry electrochemical workstation at a 3-electrode setup was used to conduct EIS analysis. Pt electrode and calomel electrode were used as a counter electrode and a reference electrode, respectively. In an electrolyte solution of 50 mM Na_2SO_4, the electrochemical analysis was carried out. EIS was seen at an open potential for 300 seconds at 0.1-105 Hz of frequency.

2. Photocatalytic Degradation of Phenanthrene

The photodegradation of PHE using the as-synthesized MIL-101(Cr) was investigated under a 500 W Xenon lamp (China) irradiation at an intensity of 450 W m^{-2}. The distance between the lamp

and the reactor is 0.50 m. As much as 30 mg of MIL-101@150 photocatalyst was added to 50 mL of PHE solution (2.0 ppm) in a beaker. Before the catalytic reaction, the solution was magnetically stirred for 30 min in the dark to attain adsorption-desorption equilibrium. The mixture was then exposed to UV light for about 150 minutes while continuously stirred. About 2 mL aliquots were withdrawn at pre-determined interval times from the solution and the residual catalyst was separated from the solution by means of centrifugation at 3,000 rpm for 5 min and returned to the reaction vessel. Finally, the absorbance of the supernatant solution was measured at 290 nm using UV-vis spectrophotometer (Jasco V-730, United States) with a 1 cm quartz cell. The supernatant was then returned to the reaction vessel. The removal efficiency (%) of the contaminant was determined as follows:

$$\text{Removal efficiency (\%)} = (C_o - C_t)/C_o * 100\% \quad (2)$$

where, C_o represents the initial concentration of PHE, and C_t is the concentration at a given time (t). The procedure was repeated for the other MIL-101(Cr) prepared at various temperatures.

The effect of the initial concentration of PHE, catalyst dosage, pH, and time of irradiation towards photodegradation was also carried out. Different catalyst dosages of 20, 30, and 40 mg were used while the other parameters were kept constant (catalyst=MIL-101@160, pH=neutral, [PHE]=2 ppm). Later, the PHE concentration was varied from 2.0 ppm to 5.0 ppm, while other conditions such as mass of MIL-101@160 (30 mg) and pH=neutral were maintained.

Similarly, the pH of the PHE solution was varied from 3 to 11 by the addition of 0.1 M HCl or 0.1 M NaOH. For this study, 30 mg of MIL-101@160 was employed with [PHE]=2 ppm.

A scavenging test was conducted to determine the active species responsible for the photocatalytic degradation of PHE. The MIL-101@160 catalyst was employed and ascorbic acid (AA, 0.1 mmol), isopropyl alcohol (IPA, 1 ml), and ethylenediaminetetraacetic acid (EDTA, 0.1 mmol) were used as scavengers for superoxide radicals ($^{\bullet}O^{2-}$), hydroxyl radicals ($^{\bullet}OH$), and positive holes (h^+), respectively. In all trials, the scavenger was added into the reaction mixture before the addition of the catalyst to allow homogeneity of the reaction. Similar procedures as for the optimum catalytic reaction above were employed.

The point of zero charge (pHpzc) of the catalyst was also determined. Six beakers containing 20 mg of MIL-101(Cr) photocatalyst were filled with 30 mL of 0.01 M NaCl solution. Then, the initial pH of the solutions was adjusted to 2, 4, 6, 8, 10, and 12 using 0.1 M NaOH or 0.1 M HCl. Afterwards, the beakers were placed inside a closed orbital shaker at 30 °C and 150 rpm for 24 h. The final pH of the solutions was measured and $\Delta pH = pH_{final} - pH_{initial}$ was plotted against the initial pH. The point where the curve intersects with the x-axis was considered as the pHpzc of the MIL-101(Cr) catalyst.

RESULTS AND DISCUSSION

1. MIL-101(Cr) Synthesis and Characterization

Fig. 1(a) depicts the IR spectrum of the terephthalic acid linker. The major peaks are located at 1,685, 1,422, 1,290, 1,106 and 933

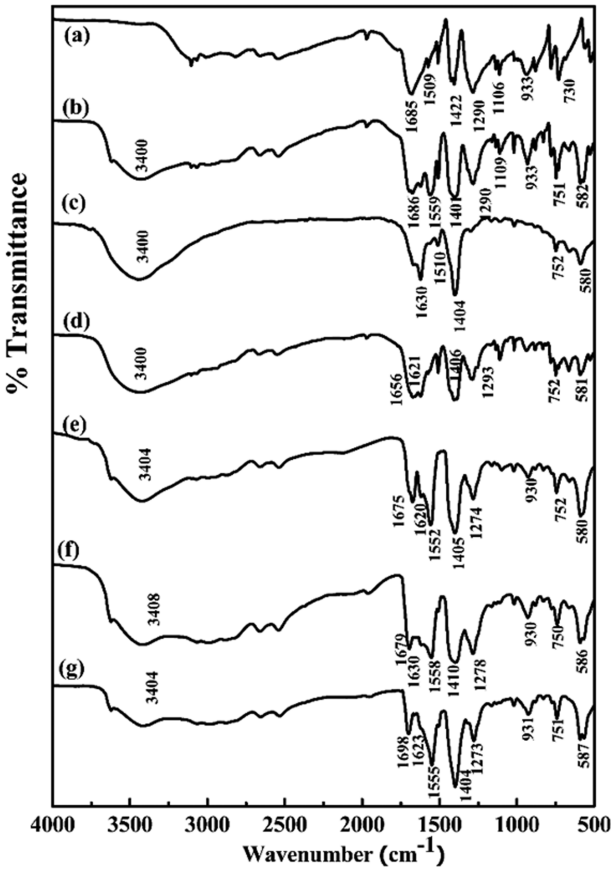

Fig. 1. FTIR spectra for (a) H_2BDC, MIL-101(Cr) synthesized at (b) 150 °C; (c) 160 °C; (d) 170 °C; (e) 180 °C; (f) 200 °C; and (g) 220 °C.

cm^{-1}. These peaks are similar to that reported by Porak and coworkers [24]. The peak at 1,685 cm^{-1} is attributed to C=O, while the peak at 933 cm^{-1} is assigned to the OH vibration of the carboxylate group [25]. Fig. 1(b)-(g) represents the FTIR spectra of MIL-101(Cr) synthesized at temperature of 150, 160, 170, 180, 200 and 220 °C, respectively. All the MIL-101(Cr) samples have shown peaks between 726 and 930 cm^{-1} assigned to the C-H stretching. Significant variation in the FTIR spectra is observed in the range of 1,290-1,700 cm^{-1} attributed to the variation in the temperature with the peak intensity increased from 150 °C to 220 °C, which further increases the nucleation of the material. The presence of the band at around 3,400 cm^{-1} in these spectra also confirms the presence of a considerable number of water molecules in the synthesized frameworks [20].

In general, the C=O peak at 1,685 cm^{-1} in H_2BDC will shift upon formation of MIL-101(Cr). This shift occurs because of the coordination of metal ions with protonated carboxylate groups. This shift to approximately 1,630 cm^{-1} is due to the interaction between the chromium atoms and the carboxylate groups of the terephthalic acid. This shift should also be accompanied by a shift in the 1,422 cm^{-1} peak to lower wavenumbers and the appearance of a peak at approximately ~580 cm^{-1}. The later peak is attributed to the vibration of Cr-O. Interestingly, it can be seen that in MIL-101@150 the peak at 1,685 cm^{-1} still exists significantly even though

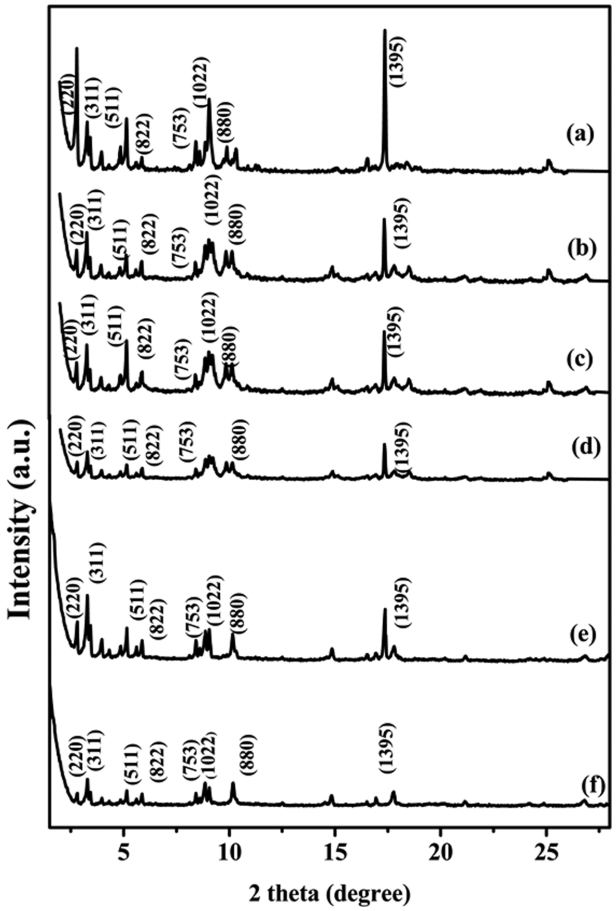

Fig. 2. PXRD Pattern of the MIL-101(Cr) synthesized at (a) 150 °C; (b) 160 °C; (c) 170 °C; (d) 180 °C; (e) 200 °C and (f) 220 °C.

another peak slightly exists at 1,630 cm^{-1}. Furthermore, a broad peak exists at 1,401 cm^{-1}. Both these occurrences indicate that although MIL-101(Cr) was synthesized, most of the carboxylate group was not protonated and coordinated with Cr.

In contrast, the MIL-101@160 demonstrated that the peak at 1,685 cm^{-1} was reduced significantly when compared to MIL-101@150. Other samples also indicated a reduction in this peak. However, its extent of reduction compared to the increase in the peak at approximately 1,630 cm^{-1} is hard to predict as several peaks seem to overlap in this region.

Fig. 2 shows the powder X-ray diffraction patterns of MIL-101(Cr) obtained at the different temperatures. As seen, the characteristic diffraction peaks occur at 2θ of 2.7°, 3.3°, 5.13°, 5.85°, 8.5°, 9.1° and 10.4°. These correspond to the Miller index of (220), (311), (511), (822), (753), (1022) and (880), respectively. There is considerable similarity between this series of MIL-101(Cr) with recently reported literature such as [26,27]. Furthermore, most of the peaks (except the peak at 2θ=17.5° ascribed to recrystallized terephthalic acid) are consistent with the simulated XRD of MIL-101 XRD patterns from its crystal structural data [27-29] Hence, this reveals the successful synthesis of the crystalline MIL-101 framework. Subsequently, the MIL101@150, MIL101@160 and MIL101@170 all give rise to sharp peaks with strong intensities. However, the intensity of the peaks decreases with increasing temperature. This indicates that the crystallite size decreases with increasing temperature. Based on Scherer's equation, the crystallite size for MIL-101@150, MIL-101@160 and MIL-101@170 is 122.5, 118 and 116 nm, respectively. Subsequently, the MIL-101(Cr) synthesized at higher temperatures exhibit even lower intensity. It has been reported that synthesis of MOF in the absence of a mineralizing agent such as HF can result in low intensity XRD peaks. This is because the presence of HF usually promotes the formation of crystalline phases by incorporation of the ions in the MOF structure [30]. Although the decrease in peak intensity with increasing temperature is not fully understood, it has been reported that the synthesis temperature can affect several factors such as the solubility of an organic ligand, its flexibility which

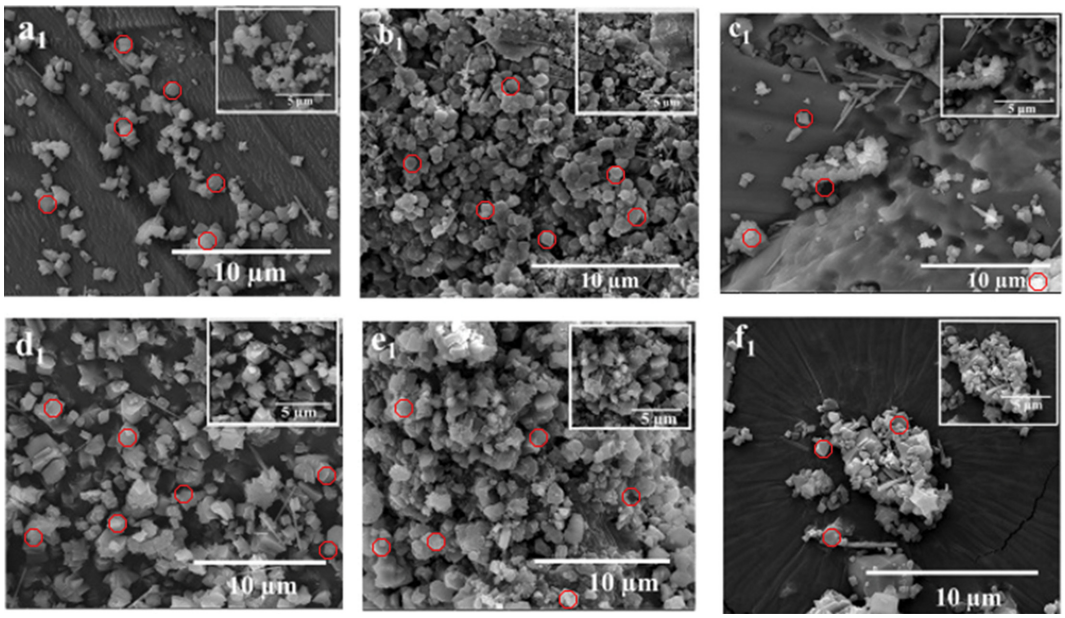

Fig. 3. SEM images of MIL-101(Cr) synthesized at (a_1) 150 °C; (b_1) 160 °C; (c_1) 170 °C; (d_1) 180 °C; (e_1) 200 °C and (f_1) 220 °C.

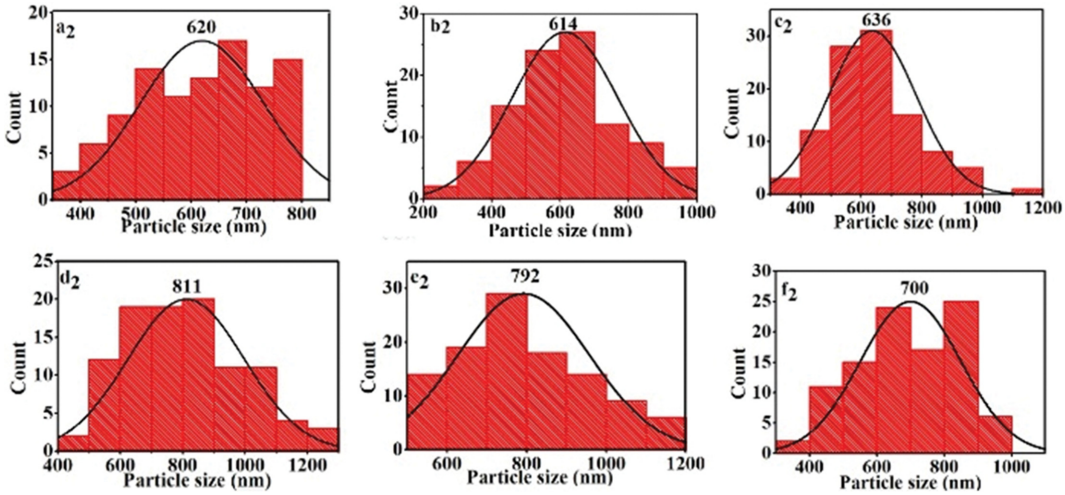

Fig. 4. Average particle sizes of MIL-101(Cr) synthesized at (a_2) 150 °C; (b_2) 160 °C; (c_2) 170 °C; (d_2) 180 °C; (e_2) 200 °C and (f_2) 220 °C.

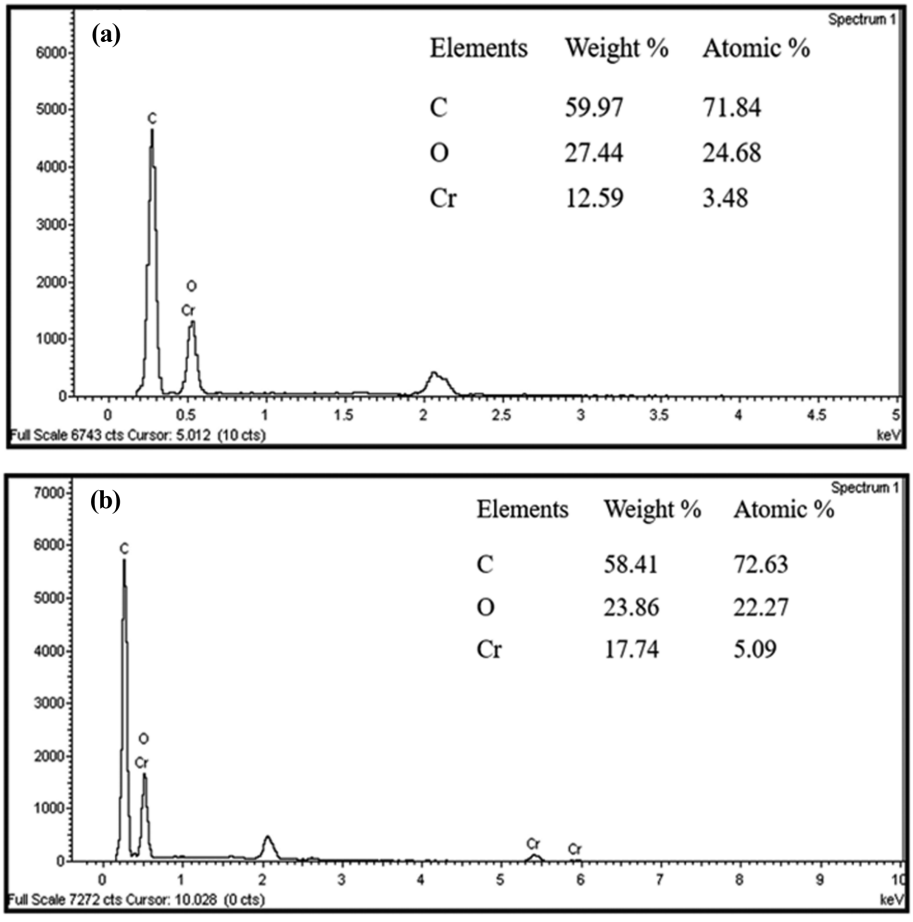

Fig. 5. EDX result of MIL-101(Cr) prepared at (a) 150 °C and (b) 220 °C.

can adopt different conformations based on the temperature, influence the coordination of organic ligands particularly the carboxylate ligand as well as the thermodynamics and kinetics of reaction during formation [31]. We believe that all these factors play a crucial role in the structure of the final MOF, which could lead to the different intensities observed in the XRD diffractogram. Other researchers have also observed similar trends [32].

SEM images of the synthesized MOFs are presented in Fig. 3. As can be seen, all the MIL-101(Cr) prepared at different temperatures exhibit particles that are octahedral in shape. Chen and co-workers [33] reported similar octahedral geometry for MIL-101(Cr) with a uniform particle size in the range of 400-600 nm

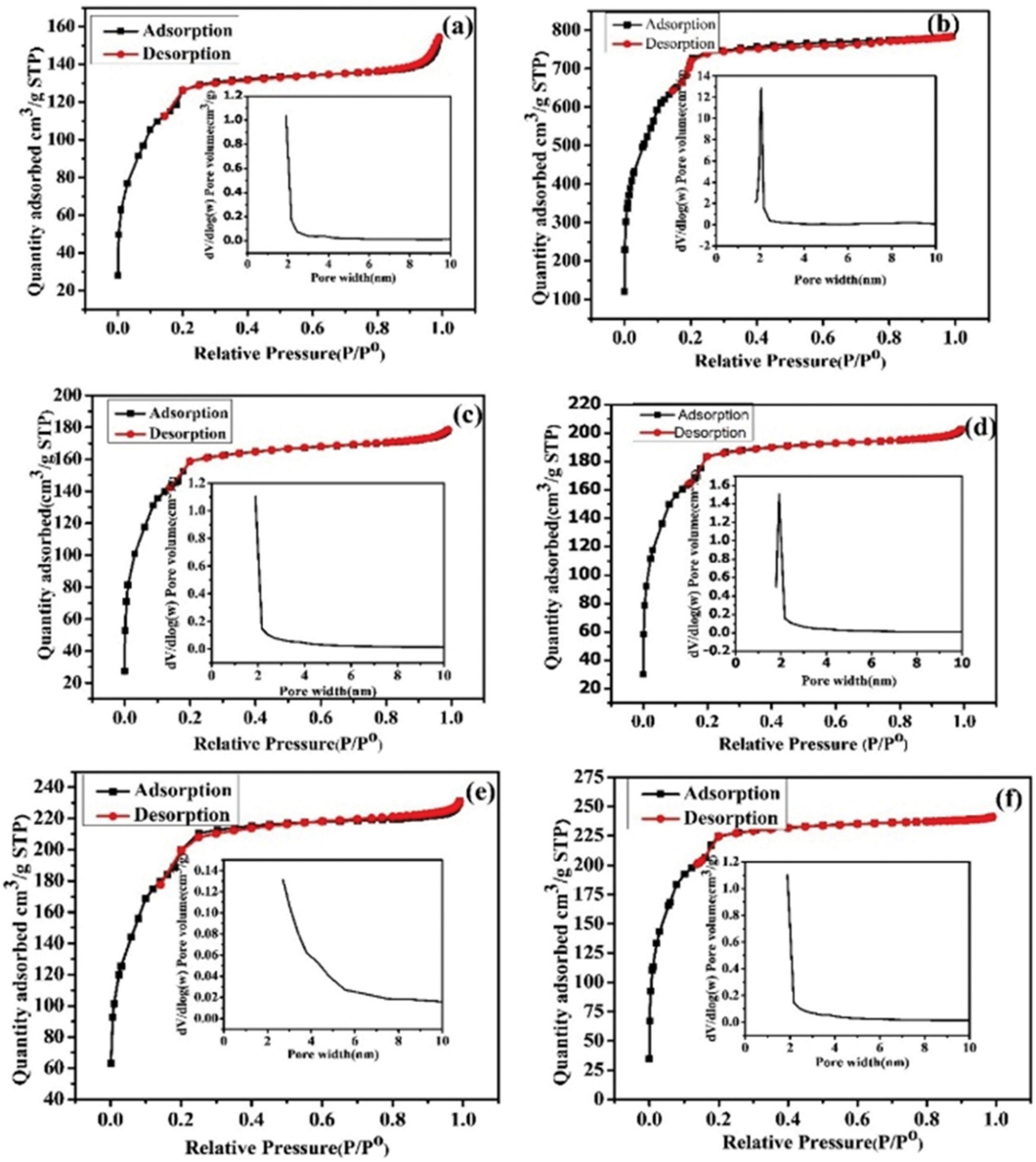

Fig. 6. Nitrogen adsorption isotherms and pore size distributions of (a) MIL-101@150, (b) MIL-101@160, (c) MIL-101@170, (d) MIL-101@180, (e) MIL-101@200 and (f) MIL-101@220.

(Fig. 4). However, in this work, some differences were observed, depending on the synthesis temperature. Apart from the octahedral morphology, the MIL-101(Cr) synthesized at temperatures 150-170 °C possessed needle-like geometry compared to MIL-101(Cr) prepared at higher temperatures. The presence of needle-like crystals in these samples could be attributed to recrystallized terephthalic acid in the MOFs [33]. The variation in the morphology of the samples can be reasonably inferred from the condition of the synthesis, that is, lower temperatures of 150, 160, and 170 °C, and short time for the synthesis compared to the previous reports in the literature [34]. Moreover, the MOFs prepared at higher temperature (180-220 °C) possessed octahedral geometry with a few needle-like particles. The octahedral geometry is visible with an average particle size in the range of 600-800 nm. The larger average size of these MIL-101(Cr) can be explained as due to the higher temperatures used, which caused particles close in contact to agglomerate and grow.

Furthermore, to confirm the distribution of the different elements in the MIL-101 series, the EDX analysis was carried out on

Table 1. Textural properties of MIL-101 series

Catalyst	BET (m^2/g)	$V_{micropore}$ (cm^3/g)
MIL-101@150	442.2	0.187
MIL-101@160	2,592.2	1.090
MIL-101@170	572.6	0.232
MIL-101@180	655.3	0.271
MIL-101@200	51.9	0.017
MIL-101@220	807.6	0.335

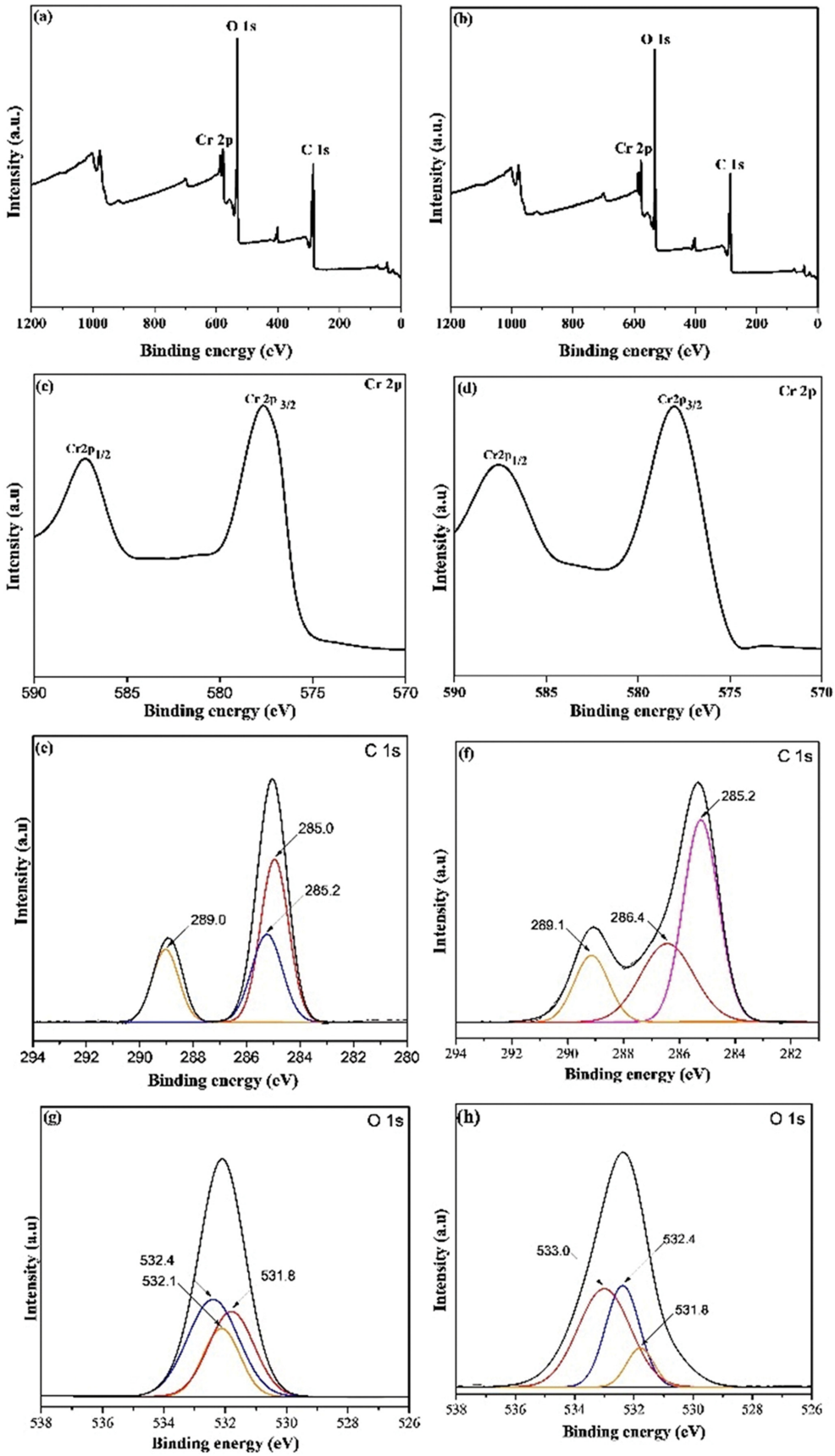

Fig. 7. XPS patterns of MIL-101@160 (a) survey, (c) Cr 2p, (e) C1s and (g) O1s spectra as well as XPS patterns of MIL-101@220, (b) survey pattern, (d) Cr 2p, (f) C 1s, (h) O 1s spectra.

MIL-101@150 and MIL-101@220 samples as representatives. Fig. 5 shows the spatial distribution of the elements in the two MIL-101(Cr) samples. As shown in Fig. 5, it is demonstrated that the elements of C, O, and Cr are uniformly distributed in the MIL-101 frameworks.

To assess the textural properties of the as-synthesized MIL-101(Cr) series, the nitrogen adsorption-desorption isotherm of the MIL-101 series was measured at 77 K (Fig. 6). Although all the MOFs were synthesized using the same procedure except for the temperature variation, their porosities demonstrated significant differences (Table 1). It was observed that all the MIL-101(Cr) exhibited microporous properties except for the MIL-101@200 catalyst. This later catalyst exhibits a mesoporous characteristic. This trend is interesting and may be explained as it is possible that the pore expanded as temperature increased. This resulted in the mesoporous nature of the MIL-101@200. However, upon further heating to 220 °C, the pore walls collapsed, resulting in the microporous nature of MIL-101@220 with a BET surface area of 807.62 m^2/g. The BET surface area of MIL-101@150 was 442.2 m^2/g, which was the lowest surface area among the series, This is attributed to the low amount of recrystallized terephthalate [35]. MIL-101@160 exhibited the highest BET surface area and largest pore volume of 2,592.2 m^2/g and 1.09 cm^2/g, respectively. This may be attributed to the attainment of the equilibrium for the formation of microporous MIL-101 material. The BET surface area decreased drastically to 572.6 m^2/g in MIL-101@170, and 655.3 m^2/g for MIL-101@180. The series shows that all the isotherms in general show a steep initial adsorption at low pressure. The almost vertical nature of the adsorption isotherm indicates that MOF is mostly microporous and has a type-I adsorption isotherm based on the IUPAC classification. However, the isotherm is not completely horizontal as it approaches P/P_o=1. This indicates the availability of mesopores, which is usually depicted by a type-IV adsorption isotherm. The MIL-101@200 shows the most mesoporous characteristic. The pore width is also shown in Fig. 6, whereas pore volume is presented in Table 1. It can be seen that for all samples, pore widths of less than 20 Å to approximately 27 Å exist. The range of the pore width varies depending on the sample, however correlates well with the isotherm observed.

XPS analyses were performed to determine chemical states of elements in MIL-101@160 and MIL-101@220. As shown in Fig. 7(a) and (b), the XPS patterns of MIL-101@160 and MIL-101@220 are similar to that of MIL-101(Cr) [13]. The survey scans show the presence of three elements: Cr, O, and C. As can be seen from Fig. 7(c) and (d), the Cr 2p XPS spectrum consists of two major peaks attributed to Cr $2p^{1/2}$ and Cr $2p^{3/2}$. These peaks are positioned around 587.24 and 577.65 eV as well as 587.67 and 577.96 eV for MIL-101@160 and MIL-101@220, respectively. These peaks correspond to the typical binding energies of Cr^{3+} [13]. This indicates that the MIL101(Cr) formed at either temperature is similar in terms of their chemical state.

Three peaks are observed in the C 1s deconvoluted XPS spectra (Fig. 7(e) and (f)). The MIL101@160 exhibit peaks at 285, 285.2 and 289 eV, while MIL101@220 gives rise to peaks at 285.2, 286.4 and 289.1 eV. The peaks at approximately 285.2 eV and 289 eV are related to carbons in terephthalate (ligand), such as aryl carbon in benzene rings and carbon in carboxyl groups, respectively. The peak at 285 eV can be attributed to the adventitious carbon [36,37], while the peak at 286.4 eV in the later catalyst can be ascribed to the C-O group [38].

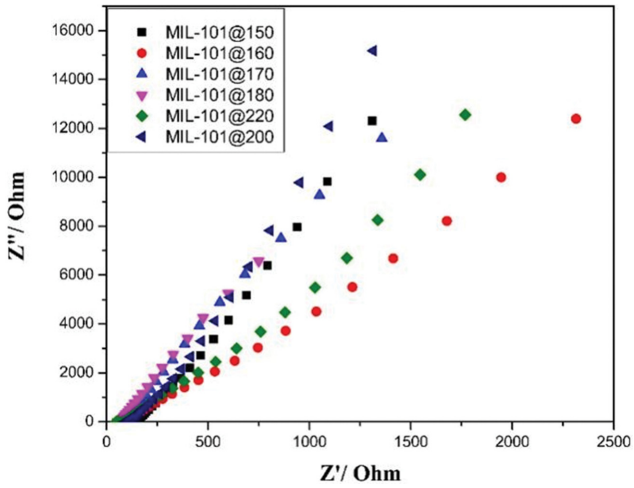

Fig. 8. EIS of MIL-101(Cr) catalysts synthesized at different temperatures.

Fig. 7((g) and (h)) presents the O 1s spectra. Deconvolution of the O1s spectra reveals that three peaks are seen. The binding energy of these peaks is 531.8, 532.4 and 533 eV for the MIL-101@220 and 531.8, 532.1 and 532.4 eV for the MIL101@160, respectively. Previous work has reported that the peak at approximately 531.8 eV is attributed to the Cr-O bond, while the peak 532.4 eV can be due to the OH group of adsorbed H_2O [36]. The binding energy of the peaks 533 eV in the MIL101@160 can be attributed to O-C=O in the terephthalate [39], while the peak at 532.1 eV in the MIL101@220 can also be attributed to carbonyl groups. The XPS result was in line with the FTIR and XRD results earlier presented.

The EIS spectra of the samples were obtained and shown in Fig. 8. In general, a large impedance is observed for the MIL-101@150, MIL-101@170, MIL-101@180 and MIL-101@200 catalysts. In contrast, a lower impedance occurs for the MIL-101@160 and MIL-101@220. This indicates that these two catalysts have a lower resistance, hence are more conductive. As such, MIL-101@160 and MIL-101@220 can facilitate better electron transfer, which is beneficial for catalytic reactions. Subsequently, the absence of a semi-circle in all the samples indicates that no charge transfer occurs in these catalysts. This can only be explained as due to the fact that the EIS analysis was not conducted under UV light. Charge transfer occurs during a photocatalytic reaction; hence, this should occur upon exposing the catalysts to the UV-light. A similar occurrence was reported by Guerrero-Araque and co-workers [40].

The thermal stability of the as-synthesized MIL-101(Cr) series was determined by thermogravimetric analysis (TGA) and presented in Fig. 9(a). Multiple weight-loss steps are observed in the TGA profiles of the MOFs as the temperature increases. The weight losses can be attributed to several factors, including the removal of water molecules and guest solvent, evaporation of the trapped water molecules in the frameworks of MIL-101(Cr) or the decomposition of the organic moieties. The initial weight loss observed

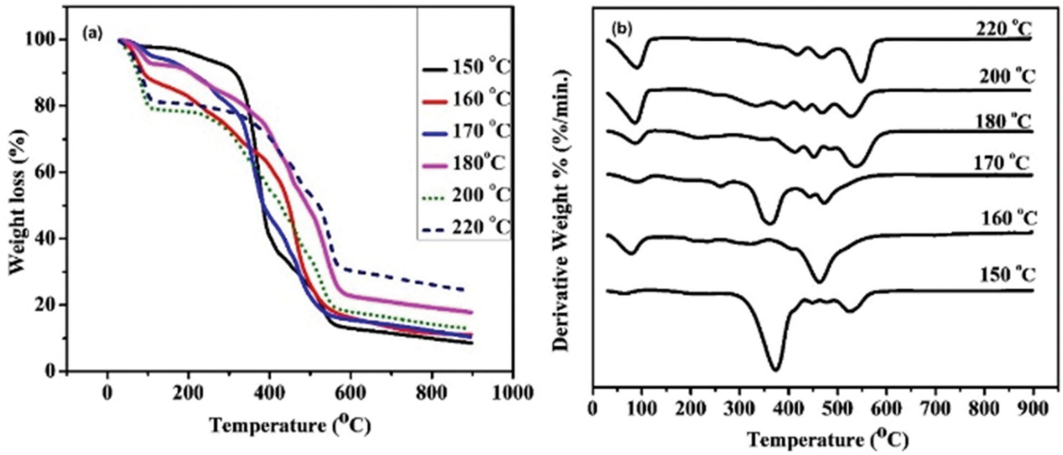

Fig. 9. (a) Thermogravimetric analysis data and (b) Differential thermal analysis of MIL-101(Cr) synthesized at different temperatures.

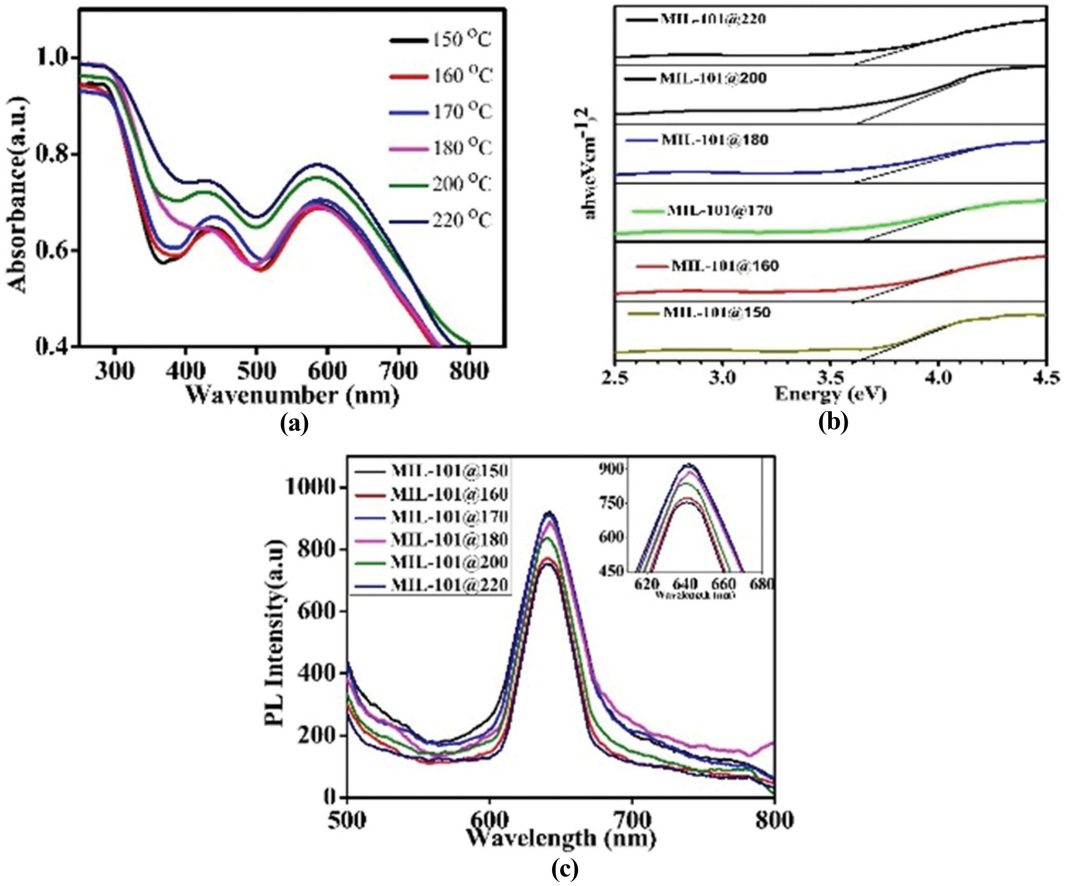

Fig. 10. (a) UV-vis DRS, (b) Tauc plots and (c) PL spectra of MIL-101(Cr) series.

in the range of 30-110 °C is typically attributed to the removal of water molecules and guest solvent. In contrast, weight loss which occurs at about 360 °C can be due to trapped water molecules [41], while higher weight loss temperatures are ascribed to the degradation of the terephthalate ligand from the MOFs framework. Furthermore, as can be seen from the DTG plot in Fig. 9(b), all the MOFs have T onset around 30 °C with corresponding T_{max} values ranging from 65 to 90 °C, which can be attributed to removal of moisture from the framework. MIL-101@150 and MIL-101@170 have similar temperature profiles with the main peak, having a T_{onset} of 275 and 285 °C with corresponding T_{max} values of 377 and 361 °C, respectively. Subsequently, MIL-101@180, MIL-101@200 and MIL-101@220 show similar degradation profiles as small degradation peaks are seen in the temperature range of 400-460 °C, which can be attributed to the removal of trapped water molecules from the framework [42]. However, main degradation peaks with

corresponding T max values of 526, 534, 526 and 547 °C were seen for MIL-101@150, MIL-101@180, MIL-101@200, and MIL-101@220, respectively. The peaks in this position can be ascribed to the degradation of terephthalate ligand from the MIL-101(Cr) framework. MIL-101@180, MIL-101@200, and MIL-101@20 have similar thermal properties. MIL-101@150 and MIL-101@170 also show similar temperature profiles; however, the intensity of the DTG peaks varies. This indicates that a higher portion of the as synthesized samples were less stable when synthesized at temperatures lower than 180 °C. Only the MIL-101@160 revealed a slightly different DTG profile. This may be reason for the different properties it exhibits.

The optical properties of the MIL-101 samples were determined using UV-Vis DRS and PL. As seen from Fig. 10(a), all the MIL-101 samples exhibit two strong absorption bands at 440 nm and 590 nm, which is in good agreement with previous reports [43]. The adsorption band at 590 nm is assigned to the absorption of the MIL-101(Cr) framework. Furthermore, the absorption in the UV-region of MIL-101(Cr) samples is attributed to the π-π* transitions of the terephthalate ligands, while the band in the visible region belongs to the d-d spin allowing the transition of the Cr^{3+} ion [44]. Moreover, the calculated band gap values of the catalysts obtained from the Tauc plot, Fig. 10(b), were all within the range of 3.60 to 3.62 which coincided with the one obtained by [43].

The PL spectrum is a useful tool for determining the electronic structure, optical characteristics, and photochemical properties of semiconductor materials, including surface oxygen vacancies and defects, as well as charge carrier entrapment, immigration, and transfer efficiency. The PL spectra of MIL-101 series are presented in Fig. 10(c). It gives clear information about the recombination rate of the charge carriers on the surface of the catalysts. The emission peaks of all the MIL-101 series were observed at 642 nm at an excitation wavelength of 320 nm. It is a well-known fact that, for a semiconductor photocatalyst to have higher photocatalytic activity, it must have a lower PL intensity, which therefore gives rise to lower recombination rate of photoinduced electron pairs [45]. Interestingly, MIL-101@150 has the highest PL intensity, while MIL-101@160 and MIL-101@220 have the lowest PL intensity. The intensity of the PL peak can indirectly be related to the synthesis temperature, which affects the structure of the final MIL-101.

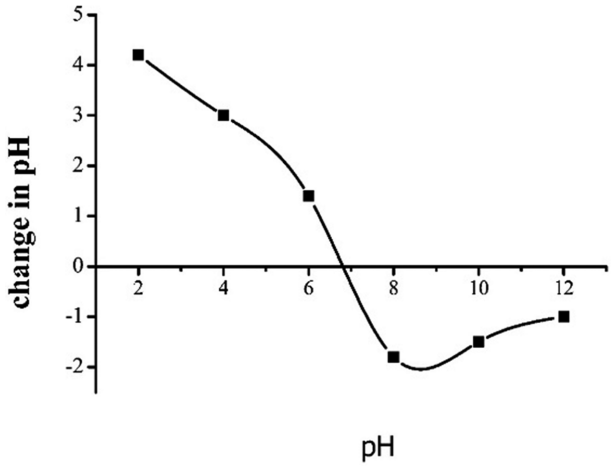

Fig. 11. Point of zero charge (pH_{pzc}) of MIL-101@160.

The point of zero charge (pH_{pzc}), which is also known as the isoelectric point, is the pH value of the catalyst at which the catalyst surface has no net charges or is neutral. The pH_{pzc} of MIL-101@160 was carried out to determine its surface charge. As shown from Fig. 11, the pH_{pzc} of synthesized MIL-101(Cr) was found to be 6.8, a similar value was obtained by [46]. When the solution pH is lower than the pH_{pzc} of MIL-101(Cr), the presence of excess H^+ ions in the solution develops positively charged and protonated sites on the surface of MIL-101(Cr). However, when the solution pH is greater than the pH_{pzc} of MIL-101(Cr), the surface of the MIL-101(Cr) photocatalyst becomes negatively charged due to the large amount of OH^- ions.

2. Photocatalytic Degradation of Phenanthrene

The photocatalytic performance of 30 mg synthesized MIL-101(Cr) samples was evaluated using the degradation of model polluted water with PHE (2 ppm, neutral pH, room temperature) under visible light irradiation (Xenon lamp 500 W). As presented in Fig. 12(a), MIL-101@160 has the highest degradation rate compared with the remaining catalysts. Particularly, 98% removal is obtained with MIL-101@160, whereas the percentage removal of 92%, 94%, 95%, 96%, and 98% was obtained after 150 mins when MIL101@150, MIL101@170, MIL101@180, MIL101@200, MIL101@220 were used, respectively.

MIL-101@160 and MIL101@220 have the highest photodegradation of PHE. This can be related to the highest BET surface area of MIL-101@160 and MIL-101@220 as well as the lower PL intensity seen in both these samples, which resulted in the lower recombination rate of photo-induced electron-hole pairs. The reason behind the enhanced photocatalytic degradation of the phenanthrene using MIL-101@160 may be because of the higher surface area and porosity. Therefore, MIL-101@160 was used for the rest of the photocatalytic studies.

The effect of the initial concentration of PHE was studied within the concentration range of 2-5 ppm using 30 mg of MIL-101@160 photocatalyst and the original pH of the solution. From Fig. 12(b) increasing the PHE concentration resulted in lowering the photodegradation efficiency. The concentration of 2.0 ppm had the highest removal of 98%, whereas 5.0 ppm, showing the lowest degradation efficiency, was 66% removal only. The decrease in the photodegradation at higher concentrations could be attributed to the blockage of the active surface of MIL-101@160 by the phenanthrene PHE [47]. Initially, most of the active sites on the MOFs are unoccupied at low PHE concentrations. As the concentration increases, many PHE molecules are available to be adsorbed on the surface of the photocatalyst. However, the number of available active sites is limited. Therefore, it would reach the maximum saturation level, and thus the % removal decreases. Similarly, when the available active sites are taken up by the PHE molecules, the adsorption of O_2 and OH^- on the MIL-101@160 photocatalyst is reduced, thereby reducing the number of radicals generated for the reaction. The competition between these species affects the efficiency of degradation. Again, since the concentration of the MIL-101@160 photocatalyst and time of irradiation was kept constant, the number of radicals produced was consistent as the concentration of the pollutant is

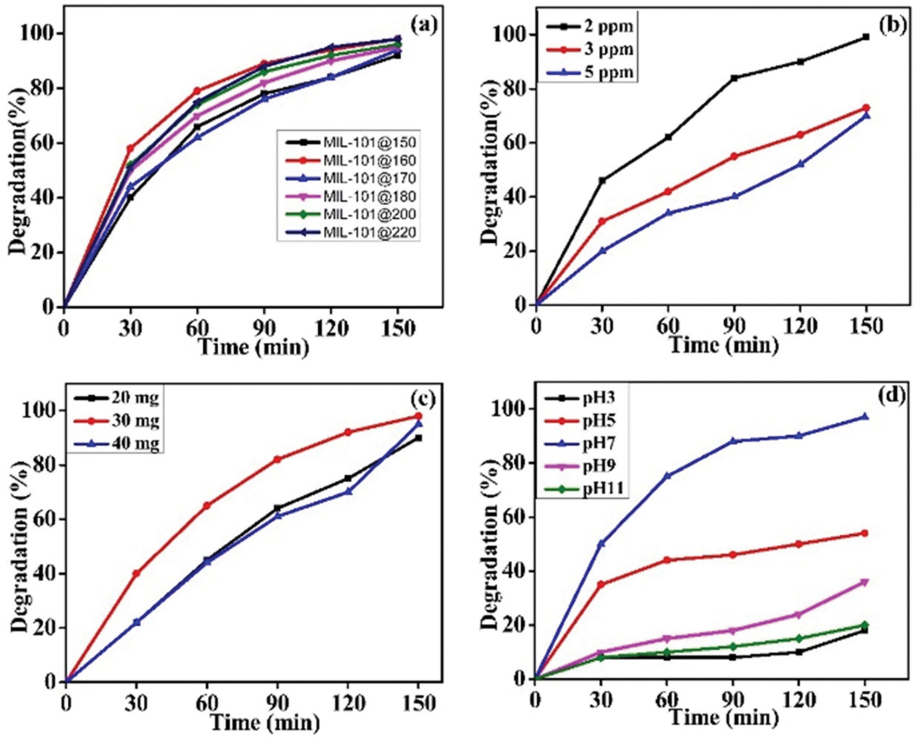

Fig. 12. (a) Degradation phenanthrene by MIL-101 samples [pH=neutral, mass of MIL-101=30 mg, [PHE]=2 ppm], (b) Effect of initial concentration [Catalyst=MIL-101@160, pH=neutral, mass of MIL-101@160=30 mg], (c) Effect of catalyst loading [Catalyst=MIL-101@160, pH=neutral, [PHE]=2 ppm], (d) Effect of pH [Catalyst=MIL-101@160, mass of MIL-101@160=30 mg, [PHE]=2 ppm].

increased. Thus, the small concentration of radicals generated was inadequate to hinder the increasing number of phenanthrene molecules as the concentration increased.

Fig. 12(c) presents the influence of the MIL-101@160 catalyst loading on the degradation of PHE by using different quantities of the photocatalyst. As can be seen in Fig. 8(c), increment of catalyst dosage from 20 to 30 mg rapidly increases the % of degradation substantially from 90% to 98% removal efficiency. Increasing the amount of MIL-101@160 from 20 to 30 mg increases the photocatalytic activity, which significantly increases the degradation efficiency. This is due to increase in light absorption and, as a result, increased production of reactive radicals, which are responsible for the degradation of PHE [33,34]. However, further increase of the photocatalyst dosage to 40 mg was found to reduce the degradation efficiency. This event may be due to the agglomeration of catalyst which limits the active sites available for the catalytic reaction. Besides, an excess amount of catalyst could also create a scattering effect by affecting the transparency of the solution, which subsequently restricts the surface area of the catalyst being exposed to light illumination and reduce the photocatalytic performance [48].

The effect of pH is one of the most important parameters in the photocatalytic process. In this study, the photodegradation of pollutant in the presence of MIL-101(Cr) samples was investigated by changing the pH from 3 to 11 with a PHE concentration of 2 ppm and photocatalyst dosage of 30 mg. This is shown in Fig. 12(d). The degradation efficiency increased from 54% to 98% by changing the pH from 5 to 7 and drastically reduced to 36% and 20% at pH 9 and 11, respectively. As pH values of the solution increased, the electrostatic attraction between the catalyst surface and phenanthrene molecules was enhanced until a maximum was reached at pH=7. Therefore, the optimum pH for the degradation of phenanthrene was found to be 7.0. The pHpzc of synthesized MIL-101@160 was measured (Fig. 11). The pHpzc was found to be 6.8. Hence, the surface charge of MIL-101@160 is negative at pH values above 6.8 and positive at values below 6.8.

It has been reported that the pKa of 3-hydroxy phenanthrene is 9.75 (strongest acid) and −5.5 (strongest base). As a similar type of molecule, (PHE) may have a close or similar pKa value. Furthermore, the protonated PHE is positively charged, hence there was probably electrostatic repulsion between the protonated PHE and positive MIL-101(Cr) may lead to the lower adsorption and photodegradation. With the increase of solution pH, the amount of positive MIL-101(Cr) decreased (Fig. 12), resulting in weaker electrostatic repulsion and an increase of PHE adsorption and photodegradation.

A kinetic study of the photocatalytic reaction is performed by fitting the experimental data for MIL-101@150, MIL-101@160, MIL-101@170, MIL-101@180, MIL-101@200 and MIL-101@220, by using a first-order model applying the following equation:

$$\frac{\mathrm{In}C_o}{C_t} = -kt \tag{3}$$

where C_o is the PHE concentration at equilibrium after a 30-minute adsorption-desorption process in dark conditions, C_t is the residual phenanthrene concentration at time t (min) in the solution, and k is the apparent rate constant in the first-order kinetic

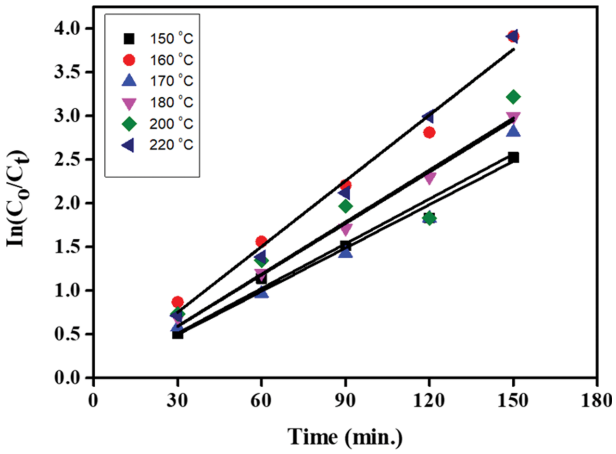

Fig. 13. In(C_o/C_t) showing pseudo-first order models for the photodegradation of phenanthrene by MIL-101(Cr) samples synthesized at different temperatures.

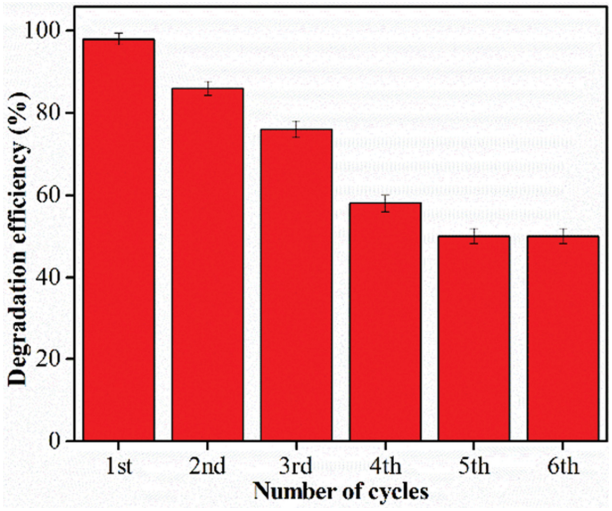

Fig. 14. Reusability of the optimized MIL-101(Cr) for the degradation of PHE.

model.

As depicted Fig. 13 and Table 2, the rate constant (k) for the MIL-101@160 and MIL-101@220 is the highest and has the same rate constant values, which is 1.52 times more than MIL-101@150 and 1.47 times higher than MIL-101@170. The higher rate constant of MIL-101@160 and MIL-101@220 photocatalysts confirms the enhanced photodegradation of PHE in solution.

The photocatalytic degradation efficiency of the PHE in various photocatalytic systems is compared in Table 3. Several materials have been reported for such applications. Most of the materials involve the use of TiO_2 and/or graphene oxide (GO). The % removal for photocatalysts containing TiO_2 is high (>80%); however, most of these materials have shown lower rate constants. In this work, in the presence of visible light irradiation, MIL-101(Cr) was clearly more efficient for photocatalytic degradation of PHE as evidenced

Table 2. Pseudo-first and second-order rate constants (k) and R^2 values obtained from the plots of InC_o/C_t and irradiation time for photodegradation of PHE using MIL-101(Cr) synthesized at different temperatures

Catalysts	First order		Second order		% Degradation
	k (min^{-1})	R^2	k (L $mol^{-1}min^{-1}$)	R^2	
MIL-101@150	0.01654	0.99825	0.02851	0.95242	92
MIL-101@160	0.0251	0.99872	0.10177	0.88287	98
MIL-101@170	0.01709	0.99552	0.03421	0.89954	94
MIL-101@180	0.01966	0.99949	0.04556	0.93583	95
MIL-101@200	0.01985	0.98901	0.05794	0.93814	96
MIL-101@220	0.0251	0.99908	0.10607	0.8879	98

Table 3. Comparison of various photocatalysts for the degradation of phenanthrene from recent literatures

Catalyst	[PHE] (ppm)	Light source	Time (min)	Catalyst dosage (mg)	% Removal	Rate constant (min^{-1})	References
Co-TiO_2-NTs-600	0.2	85 solar	600	1.0	98	6.5×10^{-3}	[49]
Pt-TiO_2-NTs	0.2	Solar-light		20	68	2.0×10^{-4}	[50]
TiO_2 graphene composite	0.5-5.0	UV light	60	25	81	NB	[51]
GO-TiO_2-$Sr(OH)_2/SrCO_3$	1.0	Solar		50		5×10^{-4}	[52]
rGO sheet	25	UV	280	2	30	NB	[53]
Dissolved organic matter fractions	2.0	250-W High P Hg Lamp		2	88-97	7.33×10^{-3}	[54]
Cu/N-codoped TiO_2	10	Visible	120	50	96	NB	[55]
Silica aeroge TiO_2	0.5	Solar	120		100	2.66×10^{-2}	[56]
MIL-101Cr @160	2.0	visible	150 min	30	98	2.51×10^{-2}	This work

NB: NA not available

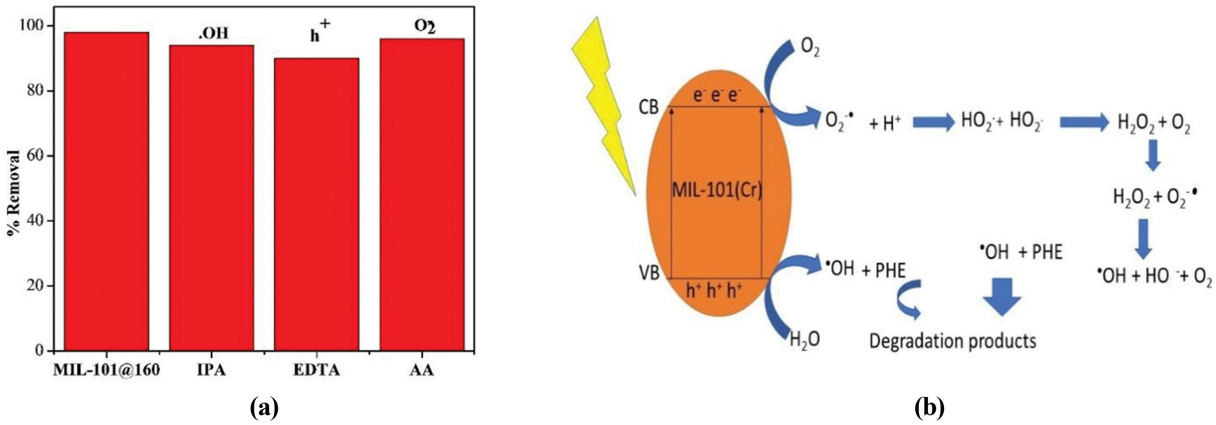

Fig. 15. (a) Effect of various scavengers on degradation of PHE and (b) PHE mechanism of degradation by MIL-101(Cr) in the presence of UV light.

by the larger rate constant ($k=2.51\times10^{-3}\ min^{-1}$). In addition, the devised system has the benefits of a low catalyst dosage (30 mg), a quick reaction time (150 min), and a high removal efficiency (98%). Therefore, the synthesized MIL-101(Cr) has a lot of potential in the wastewater treatment field.

The reusability of MIL-101 catalysts was investigated and depicted in Fig. 14. According to the findings, the photocatalyst can be recycled up to six times with a reduction efficiency of 55%. The results show that the first three cycles have better removal efficiencies. The third cycle displays removal efficiency of around 78%. The decline observed could be due to the loss of part of the catalyst during the recycling process. The removal efficiency suddenly drops to roughly 58% in the fourth and fifth cycle. This may have been the result of the catalysts' weakening absorption ability, leaching, and loss during the recovery phase.

3. Mechanism of Photocatalytic Degradation

Fig. 15(a) illustrates the effect of chemical scavengers on the photocatalytic activity of MIL-101@160. The addition of IPA and EDTA caused a decrease in the PHE removal percentage, whereas addition of AA had only a minor effect in the degradation efficiency of the catalyst. The reduction indicates that $^{\bullet}OH$ and h^+ are the main active species in the degradation, whereas $^{\bullet}O^{2-}$ played a minor role in the degradation process.

Subsequently, Fig. 15(b) depicts the schematic diagram of the proposed MIL-101(Cr) photocatalytic degradation against phenanthrene. The major steps in the photocatalytic process are enumerated below. Upon light irradiation on MIL-101(Cr), an electron (e^-) in the valence band (CB) is promoted to the conduction band through light absorption, thereby creating a positively charged hole (h^+) in the valence band. After that, the e^- and h^+ move to the catalyst's surface to start the photo-oxidation and photo-reduction reactions. So that they would not recombine again and generate heat which is not beneficial for photocatalytic reactions.

$$MIL\text{-}101@160+hv\rightarrow e^-+h^+ \quad (4)$$

Superoxide anion radicals ($O_2^{\bullet-}$) are created when O_2 molecules oxidize the excited e^- in the CB. Hydroperoxyl radicals ($HO_2\bullet$) are produced when the ($O_2^{\bullet-}$) radicals are protonated. Hydrogen peroxide (H_2O_2) is then produced as the process progresses and, lastly, hydroxyl radicals (•OH) are created. Even though the $O_2^{\bullet-}$ plays a minor role in the degradation process, however, its role in creating •OH radicals, is important for this catalytic reaction.

$$O_2+e^-\rightarrow O_2^{\bullet-} \quad (5)$$

$$O_2^{\bullet-}+H^+\rightarrow HO_2\bullet \quad (6)$$

$$HO_2\bullet+HO_2\bullet\rightarrow H_2O_2+O2 \quad (7)$$

$$H_2O_2+O_2^{\bullet-}\rightarrow\bullet OH+HO^-+O_2 \quad (8)$$

On the other hand, the positively charged h^+ in the VB reacts with water (H_2O) and hydroxyl ions (OH^-) to generate •OH radicals.

$$H_2O+h^+\rightarrow\bullet OH+H^+ \quad (9)$$

$$OH^-+h^+\rightarrow\bullet OH \quad (10)$$

The generated •OH and h^+ radicals are responsible for the degradation of PHE, thereby leading to the mineralization of the PHE into harmless species such as CO_2 and H_2O.

CONCLUSIONS

A series of MIL-101(Cr) samples were successfully synthesized at different temperatures of 10 °C intervals. The study further revealed that MIL-101(Cr) can be synthesized at a lower temperature of 160 °C without using mineral acids as additives with the highest BET surface area of 862.7 m^2/g. Nitrogen adsorption-desorption isotherm of the MIL-101 series showed a type IV isotherm with H3 hysteresis, indicating the presence of mesopores in the framework. Different catalytic loading, pollutant concentration, and the effect of pH were investigated in the photocatalytic degradation of PHE. Among the MIL-101(Cr) series synthesized, MIL-101@160 exhibited high photodegradation performance for the degradation of the PHE using visible light irradiation. Furthermore, this study revealed that the synthesized MIL-101(Cr), a porous MOF, opened a new opportunity for the synthesis and the application of the MOFs in the degradation of PAH. MIL-101(Cr), therefore serving as a promising photocatalyst that deserves serious attention for the effective removal of environmental pollutants.

REFERENCES

1. D. Gumila, Y. Zhang, Z. Shi, X. Shen, W. Cao, T. Liu, J. Liu, Q. Chen and L. Zhang, *Adv. Fiber Mater.*, **2**(1), 13 (2020).
2. Y. Sun, J. B. Mwandeje, L. M. Wangatia, F. Zabihi, J. Nedeljković and S. Yang, *Adv. Fiber Mater.*, **2**(2), 118 (2020).
3. Y. Yang, S. Zhao, F. Bi, J. Chen, Y. Wang, L. Cui, J. Xu and X. Zhang, *Appl. Catal. B: Environ.*, **315**, 121550 (2022).
4. D. Zhao and C. Cai, *Catal. Commun.*, **136**, 105910 (2020).
5. Z. Z. Uba, K. Jumbri, N. S. Sambudi, A. Ramli, N. H. H. Abu Bakar, B. Saad, M. N. H. Rozaini, H. A. Isiyaka, A. H. Jagaba, O. Aldaghri and A. Sulieman, *Polymers*, **12**, 2648 (2020).
6. N. S. Abdul Mubarak, K. Y. Foo, R. Schneider, R. M. Abdel Hameed and S. Sabar, *J. Environ. Eng.*, **10**, 106883 (2022).
7. R. Liang, F. Jing, L. Shen, N. Qin and L. Wu, *J. Hazard. Mater.*, **287**, 364 (2015).
8. Z. Xiaodong, K. Yue, R. Rao, J. Chen, Q. Liu, Y. Yang, F. Bi, Y. Wang, J. Xu and N. Liu, *Appl. Catal. B: Environ.*, **310**, 121300 (2022).
9. Z. Z. Uba, K. Jumbri, N. S. Sambudi, N. H. H. Abu Bakar, Z. N. Garba, H. A. Isiyaka and B. Saad, *Polyhedron*, **210**(9), 115515 (2021).
10. Z. Qiangyu, Q. Du, Y. Yang, Z. Zhao, J. Cheng, F. Bi, X. Shi, J. Xu and X. Zhang, *Chem. Eng. J.*, **433**, 134510 (2022).
11. N. T. Dung, N. Van Hiep, M. B. Nguyen, V. D. Thao and N. N. Huy, *Korean J. Chem. Eng.*, **38**, 2034 (2021).
12. T. Xia, Y. Lin, W. Li and M. Ju, *Chin. Chem. Lett.*, **32**, 2975 (2021).
13. J. Chen, X. Zhang, X. Shi, F. Bi, Y. Yang and Y. Wang, *J. Colloid Interface Sci.*, **579**, 37 (2020).
14. X. Zhang, Z. Zhu, R. Rao, J. Chen, X. Han, S. Jiang, Y. Yang, Y. Wang and I. Wang, *J. Environ. Sci.* (2022), https://doi.org/10.1016/j.jes.2022.03.014.
15. Z. U. Zango, K. Jumbri, H. F. M. Zaid, N. S. Sambudi and J. Matmin, *IOP Conf. Ser. Earth Environ. Sci.*, **842**, 012015 (2021).
16. F. Ruan, L. Wu, H. Yin, L. Fang, C. Tang, S. Huang, L. Fang, Z. Zuo, C. He and J. Huang, *Environ. Pollut.*, **283**, 117028 (2021).
17. N. R. Ekere, N. M. Yakubu, T. Oparanozie and J. N. Ihedioha, *J. Environ. Heal. Sci. Eng.*, **17**, 383 (2019).
18. M. Wang, S. Jia, S. H. Lee, A. Chow and M. Fang, *J. Hazard. Mater.*, **409**, 124531 (2020).
19. P. D. Du, H. T. Minh Thanh, T. C. To, H. Sy Thang, M. X. Tinh, T. N. Tuyen, T. T. Hoa and D. Q. Khieu, *J. Nanomater.*, **2019**, 6061275 (2019).
20. H. M. Gobara, R. S. Mohamed, S. A. Hassan and F. H. Khalil, *Catal. Lett.*, **146**, 1875 (2016).
21. T. K. Vo, T. P. Trinh, V. C. Nguyen and J. Kim, *J. Ind. Eng. Chem.*, **95**, 224 (2021)
22. V. Kavun, M. A. van der Veen and E. Repo, *Micropor. Mesopor. Mater.*, **312**, 110747 (2020).
23. X. Lijun, S. Liu, Z. Han, R. Jiang, H. Liu, F. Zhu, F. Zeng, C. Su and G. Ouyang, *Anal. Chim. Acta*, **853**, 303 (2015).
24. S. Porak, A. Nikseresht, M. Ali Karami and S. Ghasemi, *Res. Chem. Intermed.*, 4783 (2002).
25. Y. Wang, K. Kretschmer, J. Zhang, A. K. Mondal, X. Guo and G. Wang, *RSC Adv.*, **6**, 57098 (2016).
26. M. Mu, X. Yan, Y. Li and L. Chen, *J. Nanopart. Res.*, **19**, 148 (2017).
27. A. Farisabadi, M. Moradi, S. Borhani, S. Hajati, M. A. Kiani and S. A. Tayebifard, *J. Mater. Sci. Mater. Electron.*, **29**, 8421 (2018).
28. H. M. A. Hassan, M. A. Betiha, S. K. Mohamed, E. A. El-Sharkawy and E. A. Ahmed, *J. Mol. Liq.*, **236**, 385 (2017).
29. A. E. R. S. Khder, H. M. A. Hassan and M. S. El-Shall, *Appl. Catal. A Gen.*, **487**, 110 (2014).
30. T. Loiseau and G. Férey, *J. Fluor. Chem.*, **128**, 413 (2007).
31. Y. X. Sun and W. Y. Sun, *Chin. Chem. Lett.*, **25**, 823 (2014).
32. T. A. Mulyati, R. Ediati and A. Rosyidah, *Indones. J. Chem.*, **15**, 101 (2015).
33. H. Chen, S. Chen, X. Yuan and Y. Zhang, *Mater. Lett.*, **100**, 230 (2013).
34. N. M. Mahmoodi, M. Taghizadeh and A. Taghizadeh, *Korean J. Chem. Eng.*, **36**, 287 (2019).
35. X. Li, Y. Mao, K. Leng, G. Ye, Y. Sun and W. Xu, *Mater. Lett.*, **197**, 192 (2017).
36. T. K. Vo, J. H. Kim, H. T. Kwon and J. Kim, *J. Ind. Eng. Chem.*, **80**, 345 (2019).
37. N. Liu, F. Fei, W. Dai, J. Lei, F. Bi, B. Wang, G. Quan, X. Zhang and L. Tang, *J. Colloid Interface Sci.*, **625**, 965 (2022).
38. N. K. Gupta, J. Bae, S. Kim and K. S. Kim, *RSC Adv.*, **11**, 8951 (2002).
39. Q. Xie, Y. Li, Z. Lv, H. Zhou, X. Yang, J. Chen and H. Guo, *Sci. Rep.*, **7**, 3316 (2017).
40. D. Guerrero-Araque, P Aceved-Pena, D. Ramirez-Ortega, H. A. Calderon and R. Gomez, *Int. J. Hydrogen Energy*, **42**(12), 9744 (2017).
41. J. Shadmehr, S. Zeinali and M. Tohidi, *J. Dispers. Sci. Technol.*, **40**, 1423 (2019).
42. E. Haghighi and S. Zeinali, *RSC Adv.*, **9**, 24460 (2019).
43. H. Quan, X. Qi, J. Li, G. Liu, Y. Ning, X. Zhang, B. Zhang, Y. Fu and S. Liu, *Appl. Catal. B: Environ.*, **255**, 117751 (2019).
44. L. Wang and L. Zan, *Sci. Rep.*, **9**, 1 (2019).
45. L. Jing, Q. Yichun, W. Baiqi, L. Shudan, J. Baojiang, Y. Libin, F. Wei, F. Honggang and S. Jiazhong, *Solar Energy Mater. Solar Cells*, **90**, 1773 (2006).
46. S. Hui, J. Lv, L. Yang, L. Feng, Y. Liu, Z. Du and L. Zhang, *RSC Adv.*, **10**, 2198 (2020).
47. A. S. Belousov and E. V. Suleimanov, *Green Chem.*, **23**, 6172 (2021).
48. Khodkar, S. M. Khezri, A. Pendashteh, S. Khoramnejadian and L. Mamani, *Toxicol. Ind. Health*, **34**, 842 (2018).
49. X. Zhao, Z. Cai, T. Wang, S. E. O'Reilly, W. Liu and D. Zhao, *Appl. Catal. B: Environ.*, **187**, 134 (2016).
50. Z. Cai, X. Zhao, T. Wang, W. Liu and D. Zhao, *ACS Sust. Chem. Eng.*, **5**, 547 (2017).
51. H. Bai, J. Zhou, H. Zhang and G. Tang, *Colloids Surf. B Biointerfaces*, **150**, 68 (2017).
52. J. Fu, G. Z. Kyzas, Z. Cai, E. A. Deliyanni, W. Liu and D. Zhao, *Chem. Eng. J.*, **335**, 290 (2018).
53. A. Singh, B. Ahmed, A. Singh and A. K. Ojha, *Spectrochim. Acta - Part A Mol. Biomol. Spectrosc.*, **204**, 603 (2018).
54. S. Xue, J. Sun, Y. Liu, Z. Zhang, Y. Lin and Q. Liu, *J. Hazard. Mater.*, **361**, 30 (2019).
55. Z. Zhao, A. A. Omer, Z. Qin, S. Osman, L. Xia and R. P. Singh, *Environ. Sci. Pollut. Res.*, **27**, 17530 (2019).
56. J. Haodong, W. Liu, F. Sun, T. Huang, L. Chen, Y. Liu, J. Qi, C. Xie and D. Zhao, *Chem. Eng. J.*, **419**, 129605 (2021).